RSC Advances

ROYAL SOCIETY OF CHEMISTRY

www.rsc.org/advances

RSC Advances

RSC Publishing

ARTICLE

Synthesis of Supported Vertical NiS_2 Nanosheets for Hydrogen Evolution Reaction in Acidic and Alkaline Solution

Cite this: DOI: 10.1039/x0xx00000x

Received 00th January 2015,
Accepted 00th January 2015

DOI: 10.1039/x0xx00000x

www.rsc.org

Xiaolin Wu, Bin Yang, Zhongjian Li, Lecheng Lei, Xingwang Zhang*

We synthesized vertical NiS_2 nanosheets supported on graphite substrate, which were fabricated by the surfactant-templated reaction followed by sulfidation. These nanosheets are efficient electrocatalysts for the hydrogen evolution reaction (HER). Structural characterization revealed that the as-grown NiS_2 existed in pyrite-structure and vertical nanosheets. The NiS_2 electrocatalyst exhibited excellent activity and stability toward HER in both acidic and alkaline solution, with low Tafel slopes of ~40 and ~80 mV/decade, respectively.

1. Introduction

Due to the growing energy demands, rapid consumption of non-renewable fossil fuels, as well as increasing concerns about environment, it is urgent to explore green and sustainable energy resources. Hydrogen is considered as an ideal future fuel for its high heat of combustion and high energy capacity[1, 2]. One of the most promising methods for the production of hydrogen is water electrolysis, which obviously requires effective electrocatalysts for the hydrogen evolution reaction (HER)[3, 4]. HER catalysts are widely used under different pH conditions. Strong acidic condition is used in proton exchange membrane system[5], while alkaline water electrolysis is also widely used as basic media. Existing water electrolysis plants are usually based on cells with an aqueous alkaline electrolyte[6]. Platinum is the best known electrocatalyst for HER, but its wide-scale application is limited due to its scarcity and high cost[7].

Transition metals and their ramifications are cheap and earth-abundant, also they are potential alternative electrocatalysts for HER because of their good electrocatalytic activities. Such transition metals ramifications include Mo_2C[8], CoP[9], Ni_2P[10], MoS_2[11], WS_2[12], $MoSe_2$[13], and MoS_x[14, 15]. Recently, transition metal dichalcogenides MX_2 (where typically M = Mo, W, Fe, Co, or Ni and X = S or Se) with pyrite-structure have been identified as good HER electrocatalysts[16]. The high activity toward HER is possibly attributed to the unique pyrite crystal structure, where the metal atoms are octahedrally bonded to adjacent chalcogen atoms[17-19]. The HER behaviors of these electrocatalysts in acidic electrolyte have been investigated, however, rare of them have been proved efficient in alkaline media[20]. As with the effective catalysts of the HER in alkaline media, earth-abundant transition metal alloys[21] have been identified to be competitive, most notably Ni-based alloys[22] such as Ni-Co[23] and Ni–Mo[24, 25], whereas rare of them have poor durability and activity in acid solution. Thus, it is highly desirable to fabricate efficient HER catalysts, which can perform in a wide pH range.

With the purpose of enhancing electrocatalytic performance of HER catalysts, great efforts have been paid to optimize their composition and morphology. It is well-documented that the electrochemical properties of electrode materials are largely related to their morphology[26]. Materials with porous nanostructure can provide more active sites by providing a larger surface area compared with the plane electrode, which can facilitate the mass and electron transport to favor better HER performances[8, 27]. What's more, the nanostructured electrode facilitates the release of H_2 gas bubbles from the electrode surface to promote the stability of catalysts[19]. Lu *et al* also found porous MoS_2 film could benefit in quick removal of small H_2 gas bubbles from the electrode surface, improving the HER performance[19]. Thus, it is of great importance of develop some facile and simple methods to construct well-defined nanostructures for electrochemical performance.

Among all these transition metal dichalcogenides MX_2, few researches have been conducted over nickel sulfide. Cui *et al* synthesized NiS_2 and $NiSe_2$ nanoparticles and used them as HER catalysts, the simple HER tests of NiS_2 and $NiSe_2$ nanoparticles showed a relatively small Tafel (40-60 mV dec^{-1}) with low overpotential[17], indicating NiX_2 to be one kind of potential HER catalyst, and further investigation is still needed on the property and catalytic behavior of NiX_2.

Herein, we synthesized vertical nanosheets of NiS_2, a typical

pyrite-structure material, supported on graphite substrate (GS) by a surfactant-templated method and sulfidation. The catalyst grown on graphite revealed distinct nanostructures and showed high HER activity in both acidic and alkaline solution, exhibiting a Tafel slope of ~40 mV dec^{-1} in 0.5 M H_2SO_4 and ~80 mV dec^{-1} in 1 M NaOH. The high HER activity has been proved to be attributed to the large active surface area. The electrochemical behavior of the catalysts have been discussed over the wide pH range. In this work, it is an innovative discovery to develop a facile route to grow nanomaterials on some freestanding substrates, the method can be propagable for the fabrication of similar functional materials for various applications. Besides, developing well-adapted efficient HER catalysts composed with inexpensive earth-abundant elementals is of great importance.

2. Experimental

2.1. Materials

Sulfur powder (99.9%), nickel chloride hexahydrate ($NiCl_2 \cdot 6H_2O$), sodium dodecyl sulfate (SDS, 99.9%), urea, ethanol, graphite (99.9%), sulfuric acid, ultrapure water (18.2 MΩ·cm) are all analytical grade and were used as received without further purification.

The graphite substrates were thin graphite disks (6 mm diameter; ~0.2 mm thick), and they were sonicated in ethyl alcohol and dried in an oven at 120 °C before usage. Such graphite substrates have a geometric area of 0.2826 cm^2.

2.2. Synthesis of NiS_2 grown on graphite substrate

The NiS_2 nanosheets grown on graphite substrate (NiS_2/GS) were synthesized by a two-step method. The schematic diagram of preparation process is illustrated in **Figure 1A**. Firstly, we synthesized NiO nanosheets via a surfactant template reaction[28, 29], then NiO nanosheets grown on graphite substrate (GS) reacted with S vapor to form NiS_2.

Typically, $NiCl_2 \cdot 6H_2O$ (0.01 mol), sodium dodecyl sulfate (SDS, 0.01 mol) and urea (0.1 mol) were dissolved in 20 ml water at 40 °C to obtain green transparent solution. Then the graphite was added into the solution, reacting for another 6 h at 80 °C under magnetic stirring (*equation* 1). After the reaction, the small disks of graphite grown with $Ni(OH)_2$ were separated and washed with alternate deionized water and ethyl alcohol. As shown in **Figure 1A**, the fabrication of $Ni(OH)_2$ is of great importance during the synthesis. $Ni(OH)_2$ is probably generated by a top-down fabrication, during which SDS template played an important role for crystal growth and morphological control[30]. SDS micelles dispersed in the solution provides a conducive environment for the nucleation and growth of $Ni(OH)_2$ due to its properties of an anionic surfactant[31]. The SDS molecules absorbed onto the surface of graphite by hydrophobic groups, while counter ions connected with Ni^{2+} ions. The selective adsorption and respective counter ions of SDS directs the directional aggregation growth of $Ni(OH)_2$ with nanostructure morphology.

Then, $Ni(OH)_2$/GS were simply calcined at 300 °C in Muffle furnace to achieve nanostructured NiO/GS (*equation* 2). After the calcination, the NiO was transformed to NiS_2 in a tube reactor, the NiO/GS directly reacted with S vapor to form NiS_2/GS at 350 °C in a quartz tube reactor under argon protection (*equation* 3). The amount of the catalyst was analyzed by Atomic Absorption Spectroscopy (AAS), the average amounts of NiO and NiS_2 were 0.85 mg/cm^2 and 1.2 mg/cm^2, respectively. The molar quantity of NiO and NiS_2 were 0.011 mmol/cm^2 and 0.010 mmol/cm^2, respectively, indicating few NiO loss during the sulfidation reaction. (Detailed quantitative analysis was displayed in supporting information).

$$Ni^{2+}(aq) + 2\,OH^-(aq) \rightarrow Ni(OH)_2(s) \quad (1)$$

$$Ni(OH)_2(s) \rightarrow NiO(s) + H_2O(g) \quad (2)$$

$$2\,NiO(s) + 5S(g) \rightarrow 2\,NiS_2(s) + SO_2(g) \quad (3)$$

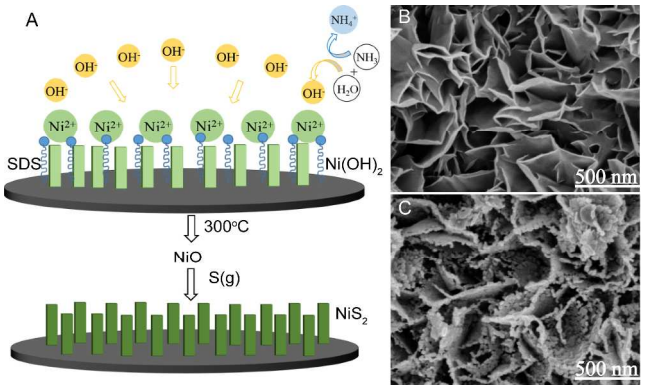

Fig.1 Synthesis of NiS_2 nanosheet on GS. (A) Schematic illustration of the synthesis of NiS_2/GS. (B) SEM image of NiO/GS. (C) SEM image of NiS_2/GS.

2.3. Characterization

The as-obtained catalysts were analyzed by scanning electron microscopy (SEM) on a SIRON-100(FEI America) field emission scanning electron microscopy. The samples were pretreated by spraying gold for 45 s. The transmission electron microscope (TEM) images were obtained by field emission transmission electron microscope (200KV/JEM-2010(HR) Japan) coupled with energy-dispersive X-ray spectrometer at an accelerating voltage of 200 kV. To prepare the specimen for TEM, the as-grown substrates were immersed in 2 mL of ethanol and sonicated for 1 min. The resulting suspension was drop casted onto a piece of a TEM grid for observation. X-ray diffraction (XRD) was carried out on a Shimadzu XRD-6000 X-ray diffractometer using Cu Kα radiation. The samples were step-scanned in steps of 0.02 ° in the range of 20-70 ° using a counter time of 24 s per step. X-ray photoelectron spectra (XPS) were obtained on Escalab 250Xi (Thermo Fisher Scientific) X-ray photoelectron spectrometer. Calibration of bingding energy was carried out by setting binding energy of C1s peak to 285.0 eV to make sure the data across samples are aligned and that the samples are not experiencing differential charging effects that may convolute the data.

2.4. Electrochemical Measurements

Electrochemical measurements were performed in a three-electrode electrochemical cell using a Bio-Logic VSP potentiostat. The measurements were performed in 100 mL 0.5 M H_2SO_4 (*aq*) electrolyte and 100 mL 1 M NaOH (*aq*) electrolyte , respectively, both were constantly purged with H_2 gas with high purity. The three-electrode electrochemical cell was consisted of a NiS_2/GS, a graphite rod and a saturated calomel (SCE), served as working electrode, counter electrode, and reference electrode (CH Instruments), respectively.

To allow potentials to be referenced against the reversible hydrogen electrode (RHE), the SCE was calibrated against the reversible hydrogen potential using platinum wire as both the

working and counter electrodes after each measurement. Linear sweep or cyclic voltammograms of samples were measured at a scan rate of 3 mV s^{-1}. Electrochemical impedance spectroscopy (EIS) was performed in potentiostatic mode from 200 kHz to 50 mHz.

3. Results

3.1. Catalyst structure and composition

To investigate the morphologies of the nanosheets of NiO and NiS_2 grown on GS, scanning electron microscopy (SEM) were performed and the images are shown in **Figure 1B** and **1C**. Homogeneous pieces with nanostructure were observed over both samples, and the NiO nanosheets were about 10 nm in thickness and arrayed. It can be inferred that the NiO nanosheets were grown onto the GS (**Figure 1B**). Interestingly, when the NiO samples transformed to NiS_2 by sulfuration, the general morphology remained unchanged, homogeneous nanosheets turned into litter particles and pieces, but the flake shapes remained (**Figure 1C**). The side view SEM images were supplied in supporting information.

TEM characterization were employed for further investigation and the images are shown in **Figure 2A** (low magnification TEM) and **Figure 2B** (High resolution TEM). In **Figure 2A**, the black particles were dispersed NiS_2 nanosheets, less than one hundred nanometers in size. The SEM and low magnification TEM images together confirm the shape and size of NiS_2——nanostructured sheets with two-dimensional structure. The high resolution TEM (HRTEM) displayed in Figure **2B** clearly demonstrates the crystal lattice, along with the fast Fourier transformation (FFT) pattern as inset, both reveal the resolved lattice fringes of NiS_2 (200) plans with a spacing of 2.83 Å, all these data are consistent with the results of XRD.

The crystal structure of NiS_2 was revealed and reconfirmed by XRD as shown in **Figure 2C**. According to the JCPDS 73-0574, the XRD pattern showed an excellent agreement with the main peaks of the standard diagram. The well-defined five peaks are centred around 2θ values of 31.45, 35.27, 38.77, 45.07 and 53.41 °, and the positions correspond to diffraction of NiS_2 with cubic pyrite phase from the (2 0 0), (2 1 0), (2 1 1), (2 2 0) and (3 1 1) reflections, respectively[32], which suggests the formation of pyrite-structure NiS_2[33].

We further investigated the electron-binding energies of Ni and S in cubic pyrite-type NiS_2 by XPS. **Figure 2D** shows the S 2p core lines of NiS_2. The strong peaks at about 162.4 eV and 163.5 eV are attributed to S $2p_{3/2}$ and S $2p_{1/2}$, respectively[34]. The Ni 2p core lines of NiS_2 are shown in **Figure 2E**, and the spectrum shows two groups of lines that originate from the spin-orbit interaction. The group at lower binding energies (BE's) and high BE's could be attributed to Ni $2p_{3/2}$ and Ni $2p_{1/2}$, respectively[35]. These XPS results further confirmed the formation of cubic pyrite-type NiS_2, which were in accord with the XRD data of the as-synthesized NiS_2.

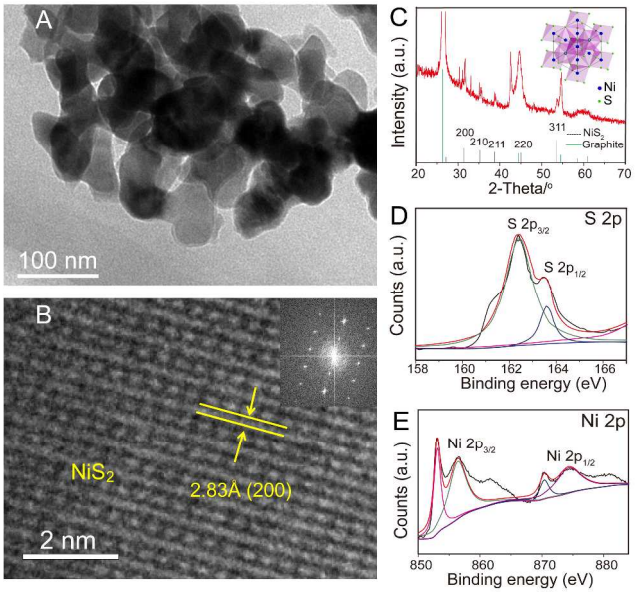

Fig.2 Structural characterization of NiS_2 in NiS_2/GS. (A) A low magnification TEM image of NiS_2. (B) A high resolution TEM image of NiS_2 catalyst and the corresponding FFT pattern as inset. (C) XRD pattern of NiS_2/GS and the crystal structure of NiS_2. XPS spectras of S 2p region (D) and Ni 2p region (E).

3.2. HER activity of catalyst in acid solution

To investigate the activities of NiS_2 toward HER in acid solution, electrochemical analysis was conducted in 0.5 M H_2SO_4 (*aq*) employing a three-electrode cell purged with H_2 (g) constantly. Pure graphite disks without loading catalysts were also tested under same condition for blank control.

Figure 3A presents the corresponding polarization curves of NiS_2/GS and blank graphite in 0.5 M H_2SO_4 after *i*R correction. The polarization curves reveal the geometric current density (*J*) plotted against the applied potential *vs.* the reversible hydrogen electrode (RHE). It is seen that the blank graphite shows negligible HER activity for the current density is quite close to 0 during the tested potential range. Whereas the NiS_2/GS electrode showed an onset overpotential at -150 mV and a low overpotential of -240 mV to achieve $J_{cathodic}$ = –10 mA cm^{-2}. Accordingly, NiS_2 gives a small Tafel slope (constructed from the linear sweep voltammograms) of 41 mV $decade^{-1}$ as shown in **Figure 3B**. As we know, the Tafel slope is commonly an inherent characteristic of the electrocatalyst, so the Tafel slope is considered as an indicator of the HER catalyst activity, a smaller Tafel slope will lead to a faster increment of the current with the increase of applied overpotential, the small Tafel slope of ~40 mV $decade^{-1}$ in this study is expected to be beneficial for practical applications. This value is very small and comparable with the best HER performance of transition metal dichalcogenides MX_2[17-19]. The excellent catalytic activity is probably due to its large active surface area, the alternative approach to estimate the effective surface area is to measure the double layer capacitance (C_{dl}) at the solid-liquid interface with cyclic voltammetry. Typically, C_{dl} is commonly is expected to be proportional to catalytically active surface area of the electrode−electrolyte interface of electron transfer in HER[36]. As shown in **Figure 3C**, by calculating the slope from the linear relationship of current density against the scan rate, the C_{dl} of NiS_2/GS electrode is 21 mF/cm^2, indicating a large active surface area of the electrode.

Stability is an important evaluation criterion in the development

of electrocatalysts. The stability of NiS_2 was evaluated by galvanostatic measurements in acid. The cathodic overpotential was required to maintain $J_{cathodic}$ = 10 mA cm^{-2} for 24 h. As shown in **Figure 3D**, a little increase of cathodic overpotential can be observed in NiS_2/GS electrode during the first several hours, which is likely due to the loss of few insecure NiS_2 in strong acid corrosion condition[17, 37]. Then the catalytic overpotential remained stable for the rest test, the increment of overpotential was no more than 40 mV from 4 h to 24 h.

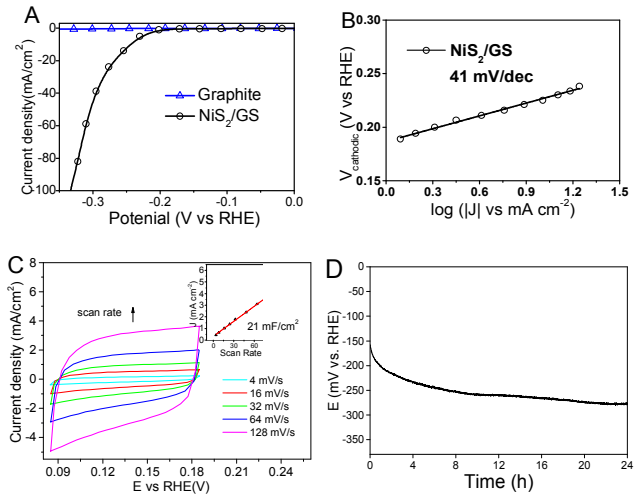

Fig.3 The HER activity of NiS_2/GS in 0.5 M H_2SO_4. (A) I-V polarization curve. (B) The Tafel plot of NiS_2 in 0.5 M H_2SO_4 derived from I-V polarization curve. (C) Cyclic voltammograms (CVs) of NiS_2/GS measured at different scan rates from 4 to 128 mV/s. Inset in (C): The plot of the current density at 0.14 V vs the scan rate. (D) Stability measurement for NiS_2/GS to maintain $J_{cathodic}$ = 10 mA cm^{-2} for 24 h.

To make an objective evaluation of the NiS_2 catalyst, several representative materials evaluated under same condition are listed in Table I for comparison. Among all these MX_2 catalysts, MoS_2 with a variety of morphologies have been extensively investigated. The 2H phase MoS_2 nanosheet exhibit a Tafel slope of ~80 mV $decade^{-1}$ with a relatively high onset potential at more than 0.25V[38]. Latest researches[39] have demonstrated that 1T MoS_2 are much more active toward HER than 2H phase, the best Tafel slope of ~40 mV $decade^{-1}$ have been achieved with a low onset potential of ~0.1V for 1T MoS_2[40, 41]. The as-synthesized NiS_2 catalyst proved competitive among these popular materials.

Table I Comparison of the HER performance with several MX_2 catalysts reported before

Materials	onset overpotential (V)	$J_{cathodic}$ = −10 mA cm^{-2} (V)	Tafel slope	Ref.
$CoSe_2$/CP	-	0.137	40	18
MoS_2/RGO	0.1	0.15	41	38
2H-MoS_2	0.25	0.35	75-85	36
2H-WS_2	0.12	0.15	138	12
3DG/CoS_x	0.11	0.33	93	40
NiS_2/GC	0.16	-	42	17
NiS_2/GS	0.15	0.24	41	Present work

CP: Carbon fiber paper; RGO: Reduced graphene oxide; 3-DG: 3-dimensional graphene; GC: glassy carbon; GS: graphite substrate.

3.3. HER activity of catalyst in alkaline solution

Since various kinds of similar materials have been tested in acid electrolyte, we mainly focused on its catalytic activity and reaction mechanism for HER in alkaline. The electrocatalytic activity was studied in 1.0 M NaOH. The polarization curves of NiS_2/GS in alkaline are displayed in **Figure 4A**. It is noteworthy that NiS_2/GS exhibited a very low onset overpotentials of about -110 mV. Moreover, the overpotentials required to approach current densities at −10, -20, -100 mA cm^{-2} were only -190, -220, and -314 mV, respectively. CVs of NiS_2/GS in alkaline were shown in **Figure 4C**, the calculated capacitance of NiS_2/GS electrode is 19.2 mF/cm^2, which is approximately equal to the capacitance in acid solution. In order to investigate the HER behavior on NiS_2/GS in 1.0 M NaOH, electrochemical impedance spectroscopy (EIS) was performed in potentiostatic mode from 200 kHz to 50 mHz. Then, we use EIS to calculate the Tafel slope and explore the proton discharging step of HER on NiS_2. Nyquist and Bode plots of the EIS response of the NiS_2/GS at various overpotentials are shown in **Figure 4C** and **4D,** respectively. As shown in **Figure 4C,** only one semicircle is observed in each Nyquist plot, indicating that the equivalent circuit for the electrocatalysis is characterized by one time constant, thus there is one unit of charge transfer resistor and a double layer capacitor in parallel.

The dependence of the phase angle -φ and the absolute values of the impedance $|Z|$ on the frequency (Bode plot) is shown in **Figure 4D,** suggesting an additional resistor element in series with the above-mentioned two elements. The Nyquist and Bode plots indicate a typical Simplified Randles Cell model as shown below[42, 43]. The model includes a solution resistance, a double layer capacitor and a charge transfer resistance.

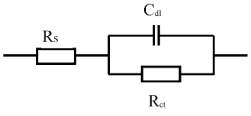

Where Rs is the series resistance of the system, including $R_{solution}$, R_{wire} and R_{GD}, can be obtained from the impedance at the high frequencies of AC impedance spectroscopy. C_{dl} and R_{ct} are the double layer capacitance and charge transfer resistance of the

electrocatalyst-electrolyte interface, respectively.The dependence of the impedance with applied potentials demonstrated that the gradient of log (R_{ct}^{-1}) versus potential corresponded to the Tafel slope of the proton discharging step[44]. The overpotential is plotted versus the inverse R_{ct} (The charge transfer resistance of the electrocatalyst-electrolyte interface (R_{ct}) at different potentials is obtained by fitting the impedance data of NiS_2/GS electrode to the corresponding equivalent circuit model mentioned above.) on a logarithmic scale, yielding a linear dependence. As shown in **Figure 4E**, the slope of ~85 mV decade^{-1} was obtained from the linear curve of η *vs* log(1/R_{ct}), and the Tafel slope of NiS_2/GS constructed from the linear sweep voltammograms in **Figure 4A** was ~80 mV decade^{-1}. Although EIS and Tafel techniques are two quite different experimental techniques, Tafel slopes obtained by both of them are qualitatively comparable. The experiments were proved to be rigorous and reliable by the mutually verified results.

The stability of NiS_2 in alkaline was also evaluated by galvanostatic measurements, the cathodic overpotential was required to maintain $J_{cathodic}$ = 10 mA cm^{-2} for 24 h. It was found in **Figure 4F** that the cathodic overpotential of NiS_2/GS fluctuated within a narrow range of less than 20 mV, suggesting NiS_2/GS was quite stable during the process in alkaline.

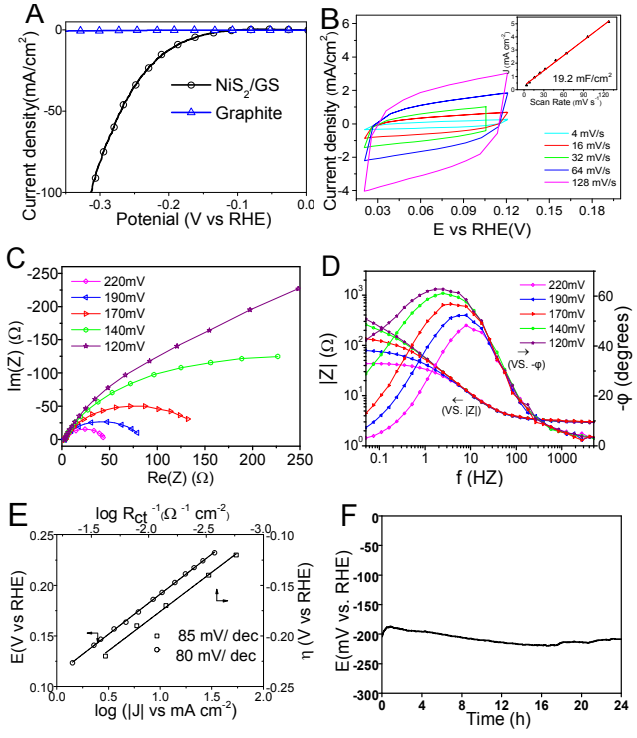

Fig.4 Electrocatalytic performance of NiS_2 samples in 1 M NaOH. (A) I-V polarization curves of NiS_2/GS and graphite. (B) Cyclic voltammograms (CVs) of NiS2/GS measured at different scan rates from 4 to 128 mV/s. Inset in (B): The plot of the current density at 0.14 V vs the scan rate. Nyquist (C) and Bode (D) plots showing EIS of NiS_2/GS at various HER overpotentials. (E) Tafel plots of NiS_2/GS in 1 M NaOH derived from I-V polarization curve and linear curve of η *vs* log (1/R_{ct}), respectively. (F) Stability measurement for NiS_2/GS, only a slight increase of 20mV was observed for a continuous catalytic current density at $J_{cathodic}$ = 10 mA cm^{-2} for 24 h.

4. Discussion

The NiS_2/GS electrode showed excellent catalytic performance and reasonable stability under acid and basic conditions for HER. The great activity of catalyst may be highly attributed to the large surface area, for the C_{dl} of NiS_2/GS is quite competitive at about 20 mF/cm^2, similar to the recently reported efficiently HER catalysts[41, 45]. Cui *et al* found that the $CoSe_2$ nanoparticle on carbon paper with higher C_{dl} at 14.1 mF/cm^2 revealed smaller Tafel slope and much lower overpotential compared with $CoSe_2$ film on glassy carbon electrode[18]. Song *et al* have explored the influence of morphology on catalyst performance[19], the C_{dl} and HER activity of CoS_2 film (3.98 mF/cm^2), microwire (14.2 mF/cm^2) and nanowire (21.5 mF/cm^2) electrodes were compared, revealing that the nanostructuring of CoS_2 showed significantly increases in its catalytic performance as the effective electrode surface area were increased, the overpotential and charge transfer resistance decreased obviously as the C_{dl} increased. These results demonstrated that the catalysts are more effective in enlarging the active surface area, meanwhile, the nanostructure of catalyst and suitable grown substrate have a positive effect in improving the active surface area of catalyst.

The HER processes on NiS_2/GS electrode were different in acid and basic condition. It is generally accepted that the HER on an electrode M may proceed through three steps in acid (equation 4-1, 5-1, 6) and alkaline (equation 4-2, 5-2, 6) solutions[46, 47], respectively:

Volmer: $M + H_3O^+ + e^- \leftrightarrow MH_{(ad)}$ (4-1)

Or: $M + H_2O + e^- \leftrightarrow MH_{(ad)} + OH^-$ (4-2)

Heyrovsky: $MH_{(ad)} + H_3O^+ + e^- \leftrightarrow H_2 + H_2O + M$ (5-1)

Or $MH_{(ad)} + H_2O + e^- \leftrightarrow M + H_2 + OH^-$ (5-2)

Tafel: $2\,MH_{(ad)} \leftrightarrow 2M + H_2$ (6)

where $MH_{(ad)}$ represents hydrogen atom adsorbed on the electrode surface.

In Volmer reaction is the electrochemical hydrogen adsorption, then followed by electrochemical desorption (Heyrovsky reaction), the final step is chemical desorption (Tafel reaction). According to previous reports, if the Tafel slope is ~118 mV decade^{-1}, the rate-determining step of the HER is Volmer reaction. While if the Tafel slope is ~40 or ~30 mV decade^{-1}, the rate-determining step would be Heyrovsky or Tafel reactions. As is shown before, the Tafel slope of NiS_2 in acid is about 40 mV decade^{-1}, the limiting step is Heyrovsky reaction, while the Tafel slopes in alkaline calculated by above two methods for NiS_2/GS (80 and 85 mV decade^{-1}) are both closer to 118 mV decade^{-1}, indicating that the Volmer reaction step is the controlling step of the HER in alkaline solution. The better catalyst activity in acid may be benefit from the pyrite-structure of NiS_2 crystal, which may facilitate the electrochemical adsorption of H atoms in Volmer step. More works such as theoretical simulation and calculation are expected to reveal the mechanism of HER over acid and basic condition on the molecular scale.

5. Conclusions

In summary, we have successfully grown vertical NiS_2 nanosheets on graphite *via* a surfactant-templated method and sulfidation. The as-synthesized NiS_2 is featured with high surface area, demonstrating homogeneous nanosheets on graphite substrate. Moreover, the NiS_2 electrocatalyst exhibited excellent activity toward HER over a wide pH range with a reasonable stability, showed low Tafel slopes of ~40 mV/decade in acidic (pH = 0) and

~80 mV/decade in alkaline solution (pH = 14), respectively. The catalytic behavior of NiS_2/GS in HER process were discussed over the different conditions. This work would encourage further research on the development of more well-adapted HER catalyst with earth-abundant elementals.

Acknowledgements

The financial support received from the Natural Science Foundation of China (Project No. 21276231, 21476201, U1462201 and U1162128).

Notes and references

[a] Key Laboratory of Biomass Chemical Engineering of Ministry of Education,
[b] College of Chemical and Biological Engineering, Zhejiang University, Hangzhou, Zhejiang Province 310027, China
[c] E-mail: xwzhang@zju.edu.cn

†Electronic Supplementary Information (ESI) available: Detailed measurement of catalyst amount, SEM images, XRD and other additional graphs.

1. A. Döner, R. Solmaz and G. Kardaş, *Int. J. Hydrogen Energy*, 2011, **36**, 7391-7397.
2. M. S. Faber and S. Jin, *Energy. Environ. Sci.*, 2014, DOI: 10.1039/C1034EE01760A.
3. W. Hu, *Int. J. Hydrogen Energy*, 2000, **25**, 111-118.
4. J. Tian, Q. Liu, A. M. Asiri and X. Sun, *J. Am. Chem. Soc.*, 2014, **136**, 7587-7590.
5. A. Le Goff, V. Artero, B. Jousselme, P. D. Tran, N. Guillet, R. Métayé, A. Fihri, S. Palacin and M. Fontecave, *Science*, 2009, **326**, 1384-1387.
6. D. Pletcher and X. Li, *Int. J. Hydrogen Energy*, 2011, **36**, 15089-15104.
7. K. Xiong, L. Li, Z. Deng, M. Xia, S. Chen, S. Tan, X. Peng, C. Duan and Z. Wei, *RSC Adv.*, 2014, **4**, 20521-20526.
8. L. Liao, S. Wang, J. Xiao, X. Bian, Y. Zhang, M. D. Scanlon, X. Hu, Y. Tang, B. Liu and H. H. Girault, *Energy. Environ. Sci.*, 2014, **7**, 387-392.
9. Q. Liu, J. Tian, W. Cui, P. Jiang, N. Cheng, A. M. Asiri and X. Sun, *Angew. Chem. Int. Ed.*, 2014, **53**, 6710-6714.
10. E. J. Popczun, J. R. McKone, C. G. Read, A. J. Biacchi, A. M. Wiltrout, N. S. Lewis and R. E. Schaak, *J. Am. Chem. Soc.*, 2013, **135**, 9267–9270.
11. T. F. Jaramillo, K. P. Jørgensen, J. Bonde, J. H. Nielsen, S. Horch and I. Chorkendorff, *Science*, 2007, **317**, 100–102.
12. Z. Wu, B. Fang, A. Bonakdarpour, A. Sun, D. P. Wilkinson and D. Wang, *Appl. Catal. B-Environ.*, 2012, **125**, 59-66.
13. C. Xu, S. J. Peng, C. L. Tan, H. X. Ang, H. T. Tan, H. Zhang and Q. Y. Yan, *J. Mater. Chem. A.*, 2014, **2**, 5597-5601.
14. D. Merki, S. Fierro, H. Vrubel and X. L. Hu, *Chem. Sci.*, 2011, **2**, 1262–1267.
15. D. J. Li, U. N. Maiti, J. Lim, D. S. Choi, W. J. Lee, Y. Oh, G. Y. Lee and S. O. Kim, *Nano Lett.*, 2014, **14**, 1228-1233.
16. H. Zhang, L. Lei and X. Zhang, *RSC Adv.*, 2014, **4**, 54344-54348.
17. D. Kong, J. J. Cha, H. Wang, H. R. Lee and Y. Cui, *Energy. Environ. Sci.*, 2013, **6**, 3553-3558.
18. D. Kong, H. Wang, Z. Lu and Y. Cui, *J. Am. Chem. Soc.*, 2014, **136**, 4897-4900.
19. M. S. Faber, R. Dziedzic, M. A. Lukowski, N. S. Kaiser, Q. Ding and S. Jin, *J. Am. Chem. Soc.*, 2014, **136**, 10053-10061.
20. X. Zou, X. Huang, A. Goswami, R. Silva, B. R. Sathe, E. Mikmeková and T. Asefa, *Angewandte Chemie*, 2014, **126**, 4461-4465.
21. A. I. Carim, F. H. Saadi, M. P. Soriaga and N. S. Lewis, *J. Mater. Chem. A.*, 2014, **2**, 13835-13839.
22. M. A. Domínguez-Crespo, A. M. Torres-Huerta, B. Brachetti-Sibaja and A. Flores-Vela, *Int. J. Hydrogen Energy*, 2011, **36**, 135-151.
23. F. Rosalbino, S. Delsante, G. Borzone and E. Angelini, *Int. J. Hydrogen Energy*, 2008, **33**, 6696-6703.
24. J. M. Jakšić, M. V. Vojnović and N. V. Krstajić, *Electrochim. Acta*, 2000, **45**, 4151-4158.
25. L. M. Rodríguez-Valdez, I. Estrada-Guel, F. Almeraya-Calderón, M. A. Neri-Flores, A. Martínez-Villafañe and R. Martínez-Sánchez, *Int. J. Hydrogen Energy*, 2004, **29**, 1141-1145.
26. D. Cai, S. Xiao, D. Wang, B. Liu, L. Wang, Y. Liu, H. Li, Y. Wang, Q. Li and T. Wang, *Electrochim. Acta*, 2014, **142**, 118-124.
27. A. B. Laursen, P. C. K. Vesborg and I. Chorkendorff, *Chem. Commun.*, 2013, **49**, 4965-4967.
28. X. Sun, G. Wang, J.-Y. Hwang and J. Lian, *J. Mater. Chem.*, 2011, **21**, 16581-16588.
29. D. Wang, Q. Wang and T. Wang, *Inorg. Chem.*, 2011, **50**, 6482-6492.
30. Z. Li, A. Gu and Q. Zhou, *Cryst. Res. Technol.*, 2009, **44**, 841-844.
31. J. Wang, Y. Xu, M. Hojamberdiev and G. Zhu, *J. Alloy. Compd.*, 2009, **487**, 358-362.
32. W.-J. Yuan, J.-C. Li, P. Chen, Y.-H. Shen and A.-J. Xie, *J. Nanopart. Res.*, 2014, **16**, 1-8.
33. H. Pang, C. Wei, X. Li, G. Li, Y. Ma, S. Li, J. Chen and J. Zhang, *Sci. Rep.*, 2014, **4**.
34. L. Yin, Y.-P. Yuan, S.-W. Cao, Z. Zhang and C. Xue, *RSC Adv.*, 2014, **4**, 6127-6132.
35. S.-L. Yang, H.-B. Yao, M.-R. Gao and S.-H. Yu, *CrystEngComm*, 2009, **11**, 1383-1390.
36. H. Zhang, B. Yang, X. Wu, Z. Li, L. Lei and X. Zhang, *ACS Appl. Mater. Interfaces*, 2015, **7**, 1772-1779.
37. H. B. Wu, B. Y. Xia, L. Yu, X.-Y. Yu and X. W. Lou, *Nat. Commun.*, 2015, **6**.
38. D. Voiry, M. Salehi, R. Silva, T. Fujita, M. Chen, T. Asefa, V. B. Shenoy, G. Eda and M. Chhowalla, *Nano Lett.*, 2013, **13**, 6222-6227.
39. H. Wang, Z. Lu, D. Kong, J. Sun, T. M. Hymel and Y. Cui, *ACS Nano*, 2014, **8**, 4940-4947.
40. Y. Li, H. Wang, L. Xie, Y. Liang, G. Hong and H. Dai, *J. Am. Chem. Soc.*, 2011, **133**, 7296-7299.
41. M. A. Lukowski, A. S. Daniel, F. Meng, A. Forticaux, L. Li and S. Jin, *J. Am. Chem. Soc.*, 2013, **135**, 10274-10277.
42. D. Merki, H. Vrubel, L. Rovelli, S. Fierro and X. Hu, *Chem. Sci.*, 2012, **3**, 2515-2525.
43. A. Damian and S. Omanovic, *J. Power Sources*, 2006, **158**, 464-476.
44. W. F. Chen, C. H. Wang, K. Sasaki, N. Marinkovic, W. Xu, J. T. Muckerman, Y. Zhu and R. R. Adzic, *Energy. Environ. Sci.*, 2013, **6**, 943-951.

45. X. Zhang, F. Meng, S. Mao, Q. Ding, M. J. Shearer, M. S. Faber, J. Chen, R. J. Hamers and S. Jin, *Energy. Environ. Sci.*, 2015, **8**, 862-868.
46. I. Danaee and S. Noori, *Int. J. Hydrogen Energy*, 2011, **36**, 12102-12111.
47. O. Aaboubi, *Int. J. Hydrogen Energy*, 2011, **36**, 4702-4709.